



www.DeepakPublishing.com

Shields, J. et al. (2017): JoSS, Vol. 6, No. 1, pp. 565–580
(Peer-reviewed article available at www.jossonline.com)



www.JoSSonline.com

Characterization of CubeSat Reaction Wheel Assemblies

Joel Shields, Christopher Pong, Kevin Lo, Laura Jones, Swati Mohan,
Chava Marom, Ian McKinley, William Wilson and Luis Andrade

*Jet Propulsion Laboratory, California Institute of Technology
Pasadena, California*

Abstract

This paper characterizes three different CubeSat reaction wheel assemblies, using measurements from a six-axis Kistler dynamometer. Two reaction wheels from Blue Canyon Technologies (BCT) with momentum capacities of 15 and 100 milli-N-m-s, and one wheel from Sinclair Interplanetary with 30 milli-N-m-s were tested. Each wheel was tested throughout its specified wheel speed range, in 50 RPM increments. Amplitude spectrums out to 500 Hz were obtained for each wheel speed. From this data, the static and dynamic imbalances were calculated, as well as the harmonic coefficients and harmonic amplitudes. This data also revealed the various structural cage modes of each wheel and the interaction of the harmonics with these modes, which is important for disturbance modeling.

Empirical time domain models of the exported force and torque for each wheel were constructed from waterfall plots. These models can be used as part of pointing simulations to predict CubeSat pointing jitter, which is currently of keen interest to the small satellite community. Analysis of the ASTERIA mission shows that the reaction wheels produce a jitter of approximately 0.1 arcsec RMS about the payload tip/tilt axes. Under the worst-case conditions of three wheels hitting a lightly damped structural resonance, the jitter can be as large as 8 arcsec RMS about the payload roll axis, which is of less importance than the other two axes.

1. Introduction

There is growing interest in the aerospace community in using small satellites as low-cost platforms for science, communication, technology development, and exploration. With this increased attention and development, small satellite capabilities are rapidly improving to meet the needs of these diverse applications (Sinclair et al., 2007). However, for science missions

in particular, attitude control performance is a key factor that limits the utility of these small platforms. Attitude control performance is affected by many elements in the system, but reaction wheel performance tends to drive pointing stability (Elias et al., 2003). Specifically, the reaction wheel imbalances are a significant contributor to pointing jitter, particularly on small spacecraft (Pong et al., 2011). Much work has been done in the past to characterize and attenuate re-

Corresponding Author: Joel F. Shields, Joel.F.Shields@jpl.nasa.gov

action wheel jitter on large structures, but the application of these models and control methodologies for CubeSats and smallsats is limited (Neat et al., 1998; Liu et al., 2008). Thus, there is interest in the smallsat attitude control community in developing accurate reaction wheel disturbance models. Vendors generally supply static and dynamic imbalance parameters, but data on the higher order harmonics is generally omitted. This paper addresses this issue by developing high fidelity models for the exported force and torque produced by the reaction wheel. Issues related to modeling of the electronics and friction are not addressed in this paper, but can be found in the following references (Bialke, 1998; Macala, 1997).

The Small Satellite Dynamics Testbed (SSDT) at the Jet Propulsion Laboratory (JPL) is a facility dedicated to the development and testing of attitude control systems (ACS) for small satellites. By providing the infrastructure and resources to promote high-fidelity dynamics simulations, early hardware-in-the-loop testing, and subsystem and system level verification and validation, the SSDT enables risk reduction and performance improvement activities that benefit small satellite projects throughout their lifecycle. The SSDT has three testing environments: a planar air bearing, a spherical air bearing, and a six degree of freedom simulation environment. The SSDT also has a hardware library of components, such as reaction wheels, star trackers, inertial measurement units, and integrated ACS units. The SSDT has undertaken a campaign to conduct detailed characterization of the components in the hardware library using test data. The test data is then used to develop models, which are integrated into the simulation for end to end performance evaluation. The use of models based on experimental data enables more accurate ACS performance evaluation and also serves to verify the specifications stated by the manufacturers. All wheels tested in this paper were tested in their pre-vibe state. Vibe testing can, however, have detrimental effects on the bearings which changes their characteristics.

This paper describes the characterization and modeling of the reaction wheel assemblies currently in the SSDT hardware library: the Blue Canyon Technology

(BCT) 15 milli-N-m-sec (purchased August 2014), BCT 100 milli-N-m-sec (purchased September 2014), and the Sinclair Interplanetary (SI) 30 milli-N-m-sec (purchased August 2014).^a These wheels were selected for inclusion in the SSDT library because they were being considered for various JPL projects and proposals at the time of purchase. As such, this collection does not represent the full spectrum of available hardware on the market, nor does it imply a JPL endorsement for these particular units or companies. The BCT wheels had 14 poles and 7 electrical revolutions per mechanical revolution, while the SI wheel had 10 poles and 5 electrical revolutions per mechanical revolution. All wheels used pulse width modulation (PWM) to drive the coils in the motor. The BCT wheels used a 20 kHz PWM signal, whereas the SI wheels used a 193 kHz PWM modulation. All wheels were tested in their standalone configuration without any external isolators or damping elements. In this sense, any comparisons among the wheels is consistent, though the actual flight performance, which would likely include isolation and damping elements, could be improved. One word of caution is that since this testing has taken place, BCT now includes a viscoelastic damper assembly that is integrated directly into the reaction wheel. Previously, this damper assembly was mounted external to the wheel.

All three of these reaction wheels were characterized on a Kistler 6-axis dynamometer, and the resulting data sets were processed and incorporated into a wheel disturbance model. This model was then integrated with the SSDT dynamics simulator and used to assess the effect of reaction wheel jitter on pointing performance for the Arcsecond Space Telescope Enabling Research in Astrophysics (ASTERIA) CubeSat mission. ASTERIA is a 6U CubeSat (approximately 10 kg, 10 x 20 x 30 cm) with the objective to achieve arcsecond-level line-of-sight pointing and highly stable temperature control of the focal plane. ASTERIA's capabilities will enable precision photometry to be performed on an opportunistic basis to study stellar activity, transiting exoplanets, and other astrophysical phenomena.

^aThe experiments with the BCT wheels were made with "rev J" of the software on the driver board, and "revision 1.3" of the NSP application was used for the Sinclair wheel.

The remainder of this paper is organized as follows. In Section 2, a review of the data acquisition system is given, followed in Section 3 by a description of the data analysis procedures. In this section, estimates of the harmonic coefficients and harmonic amplitudes are given. These parameters are incorporated into a time domain description of the exported force and torque. Section 4 displays the waterfall plots generated for each wheel, and uses the harmonic model of the BCT 15 milli-N-m-sec wheel to predict pointing performance for the ASTERIA CubeSat mission.

2. Data Acquisition System

A Kistler multicomponent piezoelectric dynamometer, type 9255C, was used to measure the exported forces and torques from each reaction wheel. This dynamometer uses four three-axis load cells to measure the applied loads on the top plate of the dynamometer. The load cell signals are further processed with a multichannel charge amplifier, type 5017A, to produce three components of force and three components of torque that are referenced to the center of the top surface of the dynamometer. The six charge amp signals are single-ended voltages that were sampled at 100 kHz with a National Instruments PXI chassis using a NI PXIe-6356 DAQ board. Each sample was quantized with 16 bits of resolution over a -10 to 10 Volt span. The gain setting of the charge amps was adjusted to make full use of the available span without incurring saturation of the voltage measurements during wheel speeds that produced resonances in the output signals. The scale factors needed to convert the sampled voltages to forces in Newtons, and torques in Newton-meters were taken from a calibration data sheet. These numbers were $1666.66e-3$ (V/N) for the F_x and F_y forces, $833.33e-3$ (V/N) for the F_z force, and $8333.33e-3$ (V/N-m) for the three torque components.

A LabView VI was developed to record and display the six sampled voltages in real time. The wheel speeds were commanded with software supplied by the manufacturer of each wheel. Rates from zero to the max speed rating for each wheel were tested in 50 RPM increments. The wheels were tested in rate feedback mode, as this is the mode that is most common in

a spacecraft ACS systems. The dwell time for each speed after reaching steady state conditions was 60 seconds, which allowed for steady state evaluation of the exported forces and torques. Separate data files for each wheel speed were generated.

The dynamometer was mounted to a 2275 kg steel seismic mass that rested upon three Newport Model SLM-24A inflatable air supports that isolated the dynamometer from ambient seismic vibrations. The Newport specifications indicate that the corner frequency of the air supports is 3–5 Hz. This isolation scheme reduced the seismic disturbances to a small amplitude relative to the wheel signals. Seismic disturbances were localized in frequency to less than 17 Hz. The first resonance of the dynamometer itself was measured to be 1800 Hz, using a PCB Piezotronics Model 086C02 impact hammer. The characterization of the wheels was thus limited to be within the range of 17 Hz and <1800 Hz.

3. Data Processing

The sampled dynamometer data was loaded into Matlab and processed to determine the harmonic and imbalance parameters for each wheel. Contour and waterfall plots were used to extract these model parameters. To remove table modes from the sampled data, which were quite large, the sampled time domain signals were subsampled. Before subsampling, the data was first filtered with a 7th order non-causal, low pass Butterworth filter with a cutoff frequency of 500 Hz. This filter removed the table modes from the signal and prevented them from being aliased to lower frequencies, which would otherwise occur with subsampling. This filtering also removed high frequency electronic noise and analog to digital quantization errors. After filtering, the data was subsampled at a rate of 1000 Hz. This provided characterization of the wheel harmonics up to 500 Hz, which is higher than previously seen in the literature and from manufacturer-provided data. To compensate for the offset between the reaction wheel center and the reference frame of the dynamometer, the moments produced by the wheel forces are subtracted from the measured moments. This gives a set of force and torque measure-

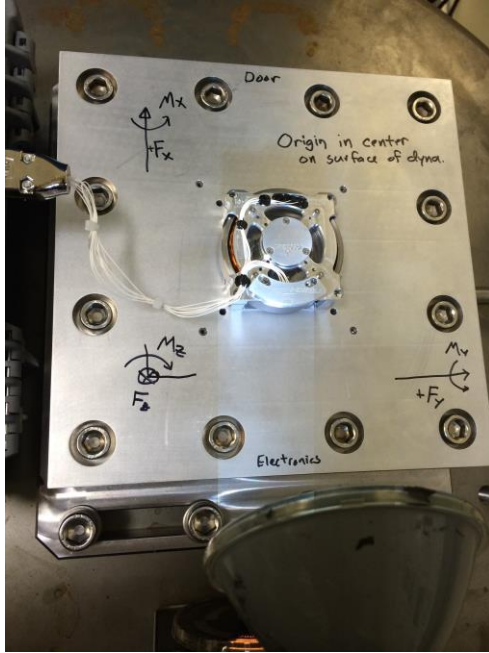


Figure 1. BCT 100 milli-N-m-s reaction wheel mounted on the interface plate of the Kistler six-axis dynamometer.

ments that are referenced to the center of the wheel assembly. The subtraction is done in the following manner:

$$M' = M_m^{TF} - v^{TF} \times F_m^{TF} \quad (1)$$

where M' are the modified moments, and M_m^{TF} and F_m^{TF} are the measured moments and forces in the table frame. The variable v^{TF} is the offset vector from the origin of the table frame to the center of the reaction wheel. The amplitude spectrums for each signal (F_x , F_y , F_z , M'_x , M'_y , M'_z) at each wheel speed were computed from the subsampled data using a 1000 point Bonham window, which is used to accurately reproduce tonal amplitudes. By grouping the spectrums for each wheel speed together, high fidelity waterfall plots for each signal were generated. These plots are shown in Section 4, Figures 5–7.

3.1. Static and Dynamic Imbalance

The static imbalance for each wheel was calculated using the fundamental harmonic of the F_x amplitude spectrum. The fundamental harmonic is defined as the ridge in the waterfall plot where the wheel speed in Hz

equals the frequency also in Hz. Any wheel speed can conceivably be used to calculate the static imbalance, but the maximum wheel speed should give the best estimate in terms of signal to noise ratio. The peak force of the fundamental at the maximum wheel speed was extracted from the F_x waterfall plot to calculate the static imbalance. The static imbalance is caused by the centripetal force, F_c , of the imbalance mass, m , as it moves about the axis of rotation:

$$F_c = ma_c = m \frac{v^2}{r} = mr\Omega^2, \quad (2)$$

where Ω is the wheel speed in radians per second and the product mr is the static imbalance in kilogram-meters (or gram-mm). The radius, r , is the radial distance of the imbalance mass from the axis of rotation. The static imbalance, mr , can be calculated by solving Eq. 2 with the peak force of the fundamental used for the centripetal force F_c and the maximum wheel speed inserted for Ω . Similarly, the dynamic imbalance is calculated from the peak torque and maximum speed of the M_x amplitude spectrum. The dynamic imbalance is caused by inclination of the principal axis of inertia relative to the axis of rotation. This inclination can be modeled as two equal and opposing imbalance masses separated by a distance d along the axis of rotation (See Figure 3). As the wheel rotates, the centripetal force of each mass causes a torque proportional to their separation distance in the plane perpendicular to the axis of rotation. This torque is given by (Macala, 1997; de Weck, 1998):

$$\tau = mrd\Omega^2. \quad (3)$$

The product mrd is the dynamic imbalance in kilogram-meters² (or gram-mm²).

3.2. Harmonic Coefficient Estimation

Estimation of the harmonic coefficients from the spectral data (waterfall plots) can be problematic due to noise in the data and closely-spaced harmonics. One technique for estimating harmonic coefficients, finding straight-line correlations of the data that pass through the origin, can successfully identify strong

tones, but has difficulty finding some of the fainter harmonics and discriminating the more closely-spaced harmonics. Hough transform techniques, which is a procedure for finding straight lines in images, had similar difficulties. As a result, instead of using numerical or image processing techniques to extract the harmonic coefficients, this analysis used visual inspection of contour plots of the spectral waterfall data to initialize estimates of the harmonic coefficients. These initial estimates were then refined using a weighted least squares solution. By properly scaling the colormap of these contour plots, the harmonic lines are clearly revealed. Visual inspection allowed one to use engineering judgment to determine the most prominent set of harmonics and in choosing the location of closely spaced harmonics.

The initial estimates can be obtained by using the Matlab cursor. Each click of the cursor gives pairwise frequency and wheel speed data. From this pair, the initial estimate of the i^{th} harmonic coefficient, h_i^o , is given by:

$$h_i^o = \frac{1}{(\Omega_i/f_i)}, \quad (4)$$

where Ω_i is the wheel speed and f_i is the frequency, both expressed in Hz. The data within a pie slice of the initial harmonic is then used to refine the estimate. The width of the pie slice is chosen big enough to capture all the data within the highlighted contour but not so big as to capture data from a neighboring harmonic. The harmonic line relating wheel speed, y , to frequency, x , is simply $y = mx$. Stacking up all the data pairs within the pie slice into vectors, \mathbf{Y} and \mathbf{X} , the least squares solution for the slope, m , is found by:

$$\hat{m} = (\mathbf{X}^T \mathbf{W}^T \mathbf{W} \mathbf{X})^{-1} \mathbf{X}^T \mathbf{W}^T \mathbf{W} \mathbf{Y}, \quad (5)$$

where the weighting matrix \mathbf{W} is diagonal consisting of the amplitude values (either force or torque) for each data point within the pie slice. The weights are necessary to center the harmonic along the spines of the amplitude data. The final estimate of the harmonic is given by,

$$\hat{h} = \frac{1}{\hat{m}}. \quad (6)$$

Figure 2a shows an example contour map with the initial and refined harmonic coefficients for each harmonic as well as the pie slice used to estimate each harmonic. This particular wheel had 38 harmonics, including two subharmonics. Note also in Figures 2a and 2b, the image of the rocking mode with positive and negative “whirls” starting at 400 Hz, and the radial translation mode at 480 Hz (Masterson et al., 2002). The harmonic coefficients consistently appeared in all six signals ($F_x, F_y, F_z, M'_x, M'_y, M'_z$), allowing one to conceivably use any of the contour plots to estimate the harmonic coefficients.

3.3. Harmonic Amplitude Estimation

Next, the amplitudes for each harmonic line must be extracted from the waterfall data. To do this, all data within a pie slice about each of the refined harmonics is again extracted from the waterfall plot. The maximum of this data set for each wheel speed bin is taken as the amplitude of the harmonic for that wheel speed. Various noise sources contaminate the amplitude data and must be mitigated. Low frequency seismic noise and line noise are the primary noise sources. These noise sources can be seen in Figure 2a. The highlighted area below 17 Hz is caused by seismic signals that make it through the isolator of the test stand. Electrical line noise at 60 Hz, 120 Hz, 180 Hz and 300 Hz can also be seen prominently in this figure. To remove the seismic and line noise, the low wheel speed amplitude data for each harmonic was replaced with a wheel speed squared polynomial segment which insured a zero amplitude at zero wheel speed. This removed the seismic noise which contaminated the low wheel speed region of each harmonic. In addition, this polynomial segment replaced the line noises at 60 Hz, 120 Hz, 180 Hz and 300 Hz when they intersected the harmonic at low wheel speeds.

Figure 2b shows the extracted amplitude data for each harmonic of the BCT 15 milli-N-m-s F_x signal highlighted in green. Linear interpolation is used to find the amplitude between wheel speed bins. Due to sampling rate limitations, some of the higher order harmonics will not have amplitude data for the higher wheel speeds. Looking at Figure 2a, for example, the harmonics that intersect the right hand side of the plot

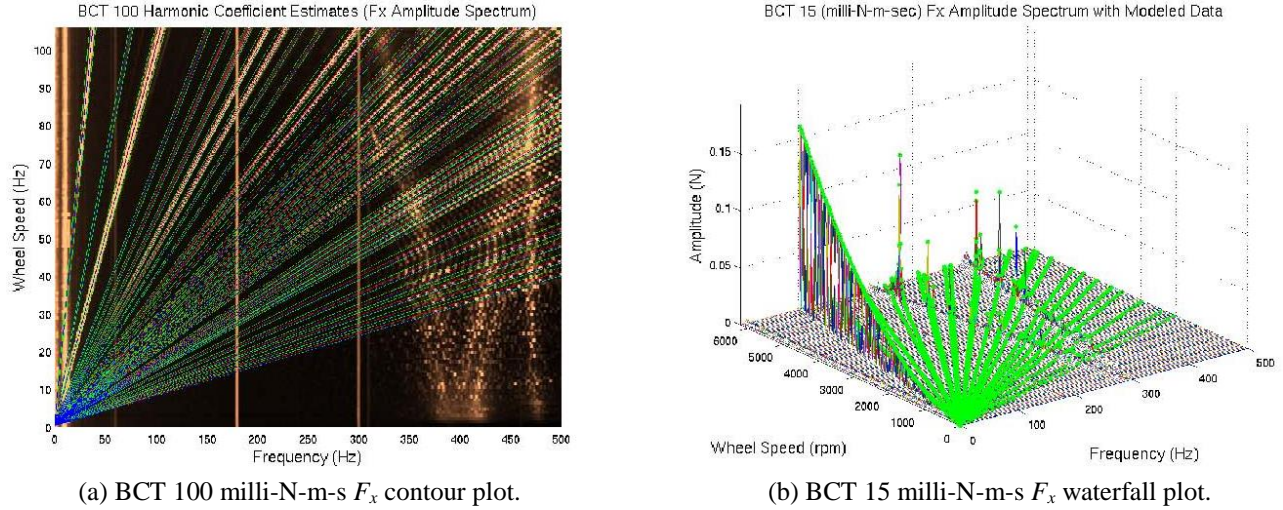


Figure 2. (a) Contour plot of the F_x signal for the BCT 100 milli-N-m-s reaction wheel, showing the initial estimate of the harmonic coefficients in red, the refined estimates in blue, and the sector of data used to refine the initial estimates in green. (b) Waterfall plot for the BCT 15 milli-N-m-s F_x signal with the harmonic amplitude data highlighted in green.

at 500 Hz are not defined over all possible wheel speeds. For the most part, this is a benign issue, as the amplitudes tend to be small and can be safely approximated as zero beyond the 500 Hz Nyquist frequency. For some signals, structural cage modes can cause the harmonic amplitudes to resonate near 500 Hz in which case the sample rate should be increased to fully capture the amplitudes without the need for extrapolation. This study used the Matlab function `interp1()` for handling wheel speeds that intersect the harmonic beyond the Nyquist rate, as it has an option for specifying zero output beyond the domain of a given data set.

With the harmonic coefficients and harmonic amplitudes for each harmonic extracted from the waterfall plots, a time domain representation of the three exported forces and three exported torques can be written as:

$$F_x(t) = \sum_{i=1}^{N_h} F_{x_i}(\Omega(t)) \cdot \sin(2\pi h_i \Omega(t)t + \phi_i^{F_{rad}}) \quad (7)$$

$$F_y(t) = \sum_{i=1}^{N_h} F_{y_i}(\Omega(t)) \cdot \sin(2\pi h_i \Omega(t)t + \phi_i^{F_{rad}} + \frac{\pi}{2}) \quad (8)$$

$$F_z(t) = \sum_{i=1}^{N_h} F_{z_i}(\Omega(t)) \cdot \sin(2\pi h_i \Omega(t)t + \phi_i^{F_{axial}}) \quad (9)$$

$$M_x(t) = \sum_{i=1}^{N_h} M_{x_i}(\Omega(t)) \cdot \sin(2\pi h_i \Omega(t)t + \phi_i^{M_{rad}}) \quad (10)$$

$$M_y(t) = \sum_{i=1}^{N_h} M_{y_i}(\Omega(t)) \cdot \sin(2\pi h_i \Omega(t)t + \phi_i^{M_{rad}} + \frac{\pi}{2}) \quad (11)$$

$$M_z(t) = \sum_{i=1}^{N_h} M_{z_i}(\Omega(t)) \cdot \sin(2\pi h_i \Omega(t)t + \phi_i^{M_{axial}}) \quad (12)$$

where $\Omega(t)$ is the wheel speed in Hz, h_i are the harmonic coefficients and $\phi_i^{F_{rad}}$, $\phi_i^{F_{axial}}$, $\phi_i^{M_{rad}}$, and $\phi_i^{M_{axial}}$ are the initial phases of each harmonic for the force or moment component indicated. $F_{x_i}(\Omega(t)) \dots M_{z_i}(\Omega(t))$ are the harmonic amplitudes associated with each harmonic. In principle, both $F_{x_i}(\Omega(t)) = F_{y_i}(\Omega(t))$

and $M_{x_i}(\Omega(t)) = M_{y_i}(\Omega(t))$, but they have been kept as unique variables, since the dynamometer has slightly different accuracy in these two directions. Conceivably, one could take advantage of this constraint and take the average of the x and y components to form a “radial” harmonic amplitude for the force and torque, but no effort was made here to do that. Note that the structure of the harmonic amplitudes was left unspecified. For many of the harmonics, in particular the fundamental, the harmonic amplitude is accurately modeled as being proportional to $\Omega^2(t)$. When harmonics transit the various structural cage modes of the wheel assembly, this is not the case, so the dependence on $\Omega(t)$ has been left unspecified. Eq. 8 has 90 degrees of phase added to it to account for the fact that the F_x and F_y forces will always be out of phase by this amount. Likewise, Eqs. 10 and 11 also have 90 degrees of phase difference. The phases in Eqs. 7–12 are taken from a uniform distribution from $[0, 2\pi]$, though conceivably they could be estimated from the time series data. A graphical model of the planar forces and torques described by Eqs. 7–8 and 10–11 is shown in Figure 3. Each mass for the static imbalance and each pair of masses for the dynamic imbalance rotates at a rate dependent on the wheel speed and harmonic coefficient. Figure 4 shows a sample time series generated from Eqs. 7–12 using the Sinclair Interplanetary reaction wheel model.

4. Results

Table 1 summarizes the static and dynamic imbalances for each wheel tested. The dynamic imbalances for the BCT 100 and BCT 15 wheels listed in Table 1 were 3.8 and 6 times larger, respectively, than those listed in the specification sheets for these wheels. The SI 30 wheel did not list the dynamic imbalance on its specification sheet. These discrepancies may be a result of updates to the specifications since the purchase of the unit, unit-to-unit variation, or differences in measurement techniques. The magnitude of this difference between current specification and measured performance underscores the need for this type of testing, particularly for missions that are sensitive to jitter. One might expect the imbalances to scale with the momentum capacity of the wheel. The BCT 100 wheel, however, was ordered with a “fine balancing” option, which resulted in better performance. The dynamic imbalance of this wheel is actually smaller than that of the Sinclair Interplanetary wheel in spite of its much larger momentum capacity, and the static imbalance is only marginally bigger than the Sinclair wheel. This table serves as a quick reference for determining the imbalance quality of each wheel. More detailed performance characteristics can be ascertained by looking at the waterfall plots in Figures 5–7. Each of these

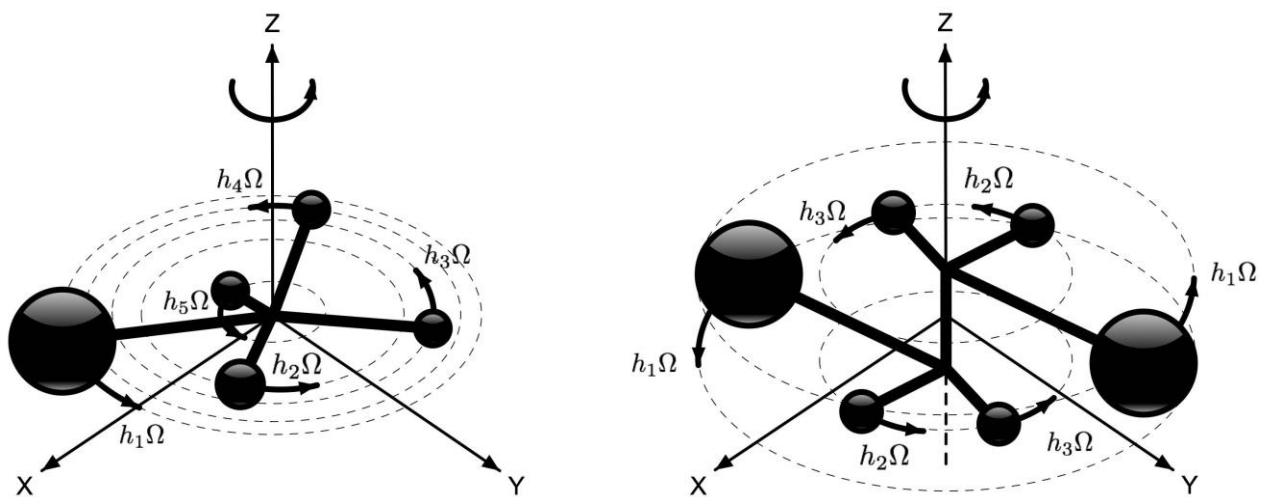


Figure 3. Graphical depiction of the reaction wheel disturbance model showing the first five harmonics of the static imbalance on the left and first three harmonics of the dynamic imbalance on the right. Each harmonic of the static imbalance is characterized by a mass at a given radius and a rotation frequency $h_i\Omega$. Each harmonic of the dynamic imbalance consists of two mass opposite each other with a vertical distance d separating the two masses. This separation creates a moment due to the centripetal force on each mass that precesses with the rotation.

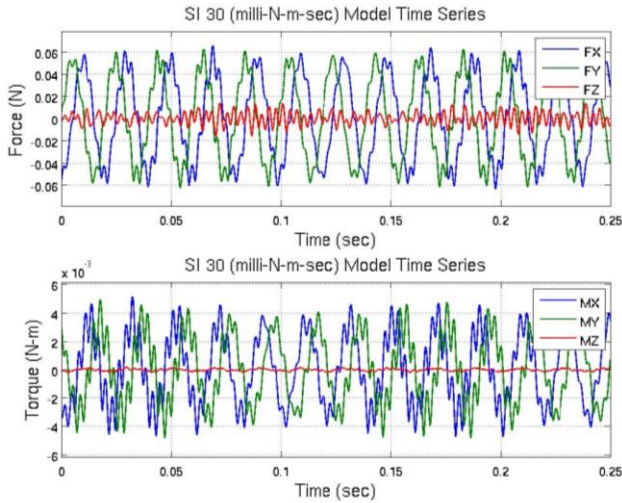


Figure 4. Modeled time series for the Sinclair Interplanetary 30 milli-N-m-s reaction wheel using a wheel speed of 3000 RPM.

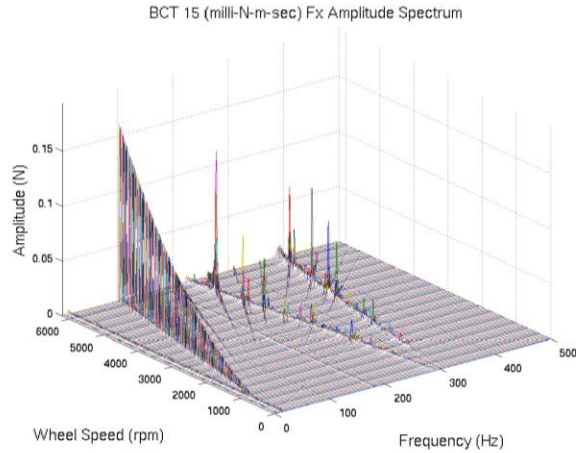
figures gives the three exported force signals and three exported torque signals for each wheel. These plots not only show the static and dynamic imbalances which can be extracted from the fundamental harmonic, but also the various structural cage modes of each wheel. These modes include the axial translation mode, an example of which can be seen in Figure 6e at 480 Hz and to a lesser extent in Figure 5e at 385 Hz, the radial translation mode which appears in Figures 6a and 6b, and the rocking mode which can be seen as the “V” in Figures 5a–f, 6a–d, and 7a–d. The interaction of the higher harmonics with these structural cage modes must be modeled to accurately predict the disturbance forces and torques produced by each wheel. As can be seen in these figures, there are wheel speeds where the amplitude of the higher harmonics interacting with the structural cage modes can be a significant portion of or even exceed the amplitude of the fundamental harmonic. Note that the amplitude of the fundamental harmonic in Figures 5–7 is proportional to the square of the wheel speed, as would be predicted by Eq. 2. This

is actually a good model for the sub and higher harmonics, were it not for the amplifications due to the structural cage modes.

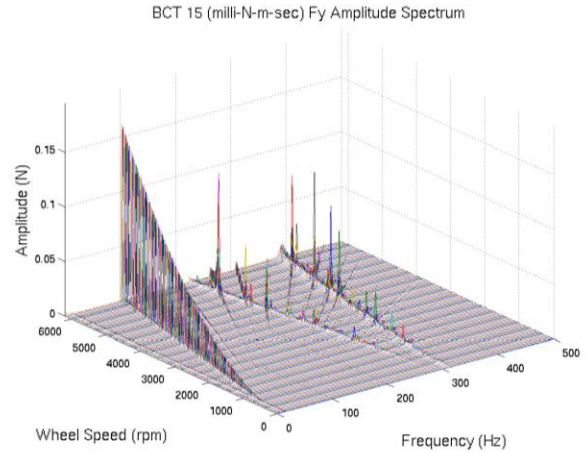
These figures also show the impact of seismic and line noise on the data sets. For the F_x , F_y , M_x and M_y signals, these noises are relatively small compared to the signal levels. They do, however, have a significant impact on the F_z and M_z signals, since the amplitude of these signals is smaller. Looking at Figures 5e–f, Figures 6e–f, and Figures 7e–f one can observe the low frequency (< 17 Hz) seismic noise and line noises at 60 Hz, 120 Hz, 180 Hz, and 300 Hz. Aside from the fundamental harmonic, the most prominent feature of these figures is the rocking mode, which is caused by flexibility in the bearing mount in the tip and tilt directions of the flywheel. When the higher harmonics cross the rocking mode, the disturbance signals are amplified. In particular, if the damping of the rocking mode, or any other mode, is poor, significant disturbance signals can result. The two BCT wheels seem to have less damping in this regard, as compared to the Sinclair wheel. In particular, the F_z signal for the BCT 100 wheel has significant resonances when the higher harmonics cross the axial translation mode at 480 Hz. The disturbance force from this mode can be twice the peak fundamental force for wheel speeds near 3000 RPM and 4000 RPM (See Figure 6e.). The location of this axial mode demonstrates the need to characterize these wheels at as high a frequency as possible. The axial translation mode of the BCT 100 wheel at 480 Hz would not have been revealed otherwise. Although the F_z force can be large, its contribution to rigid body rotations of the spacecraft would depend on the wheel placement relative to the center of mass and on the mass properties of the spacecraft. A disturbance at 480 Hz, for example, would have about 25 times less of an effect on spacecraft pointing than a disturbance at 100 Hz because of the double integrator plant. The effect

Table 1. Summary of Reaction Wheel Imbalances

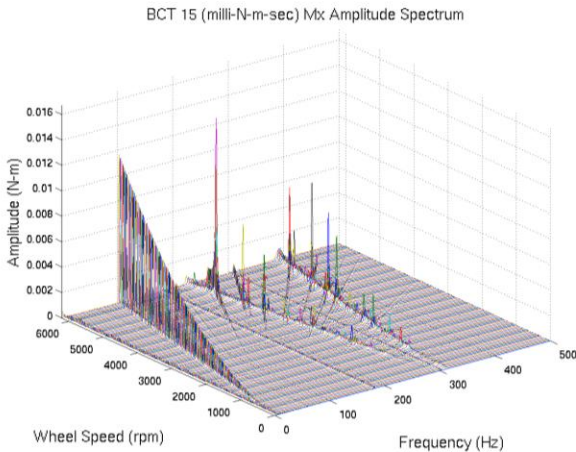
Wheel	Momentum Capacity (milli-N-m-s)	Static Imbalance (gram-mm)		Dynamic Imbalance (gram-mm ²)	
		Measured	Spec. Sheet	Measured	Spec. Sheet
BCT 15	15	0.38	≤ 0.35	27.59	≤ 4.55
BCT 100	100	0.69	≤ 0.50	33.12	≤ 8.58
SI 30	30	0.65	NA	43.16	NA



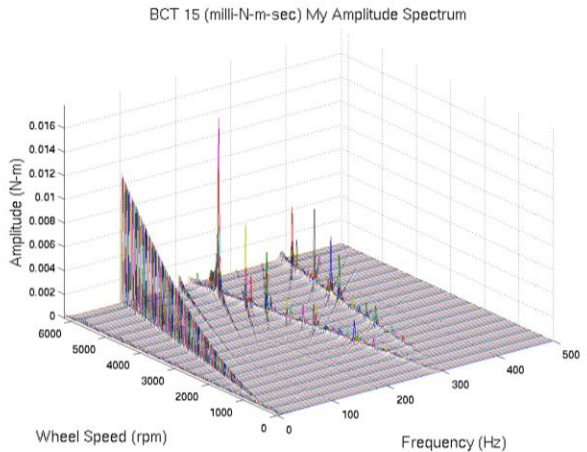
(a) F_x waterfall.



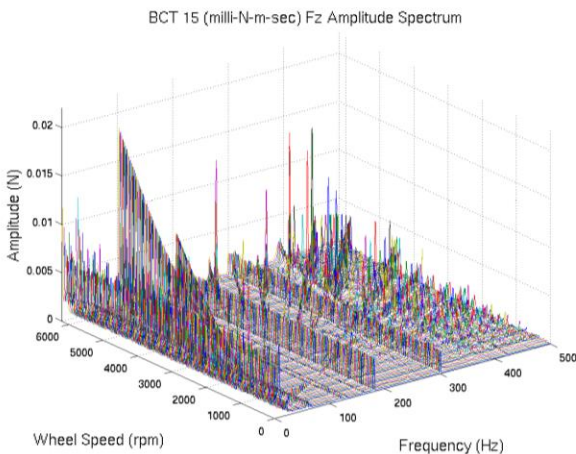
(b) F_y waterfall.



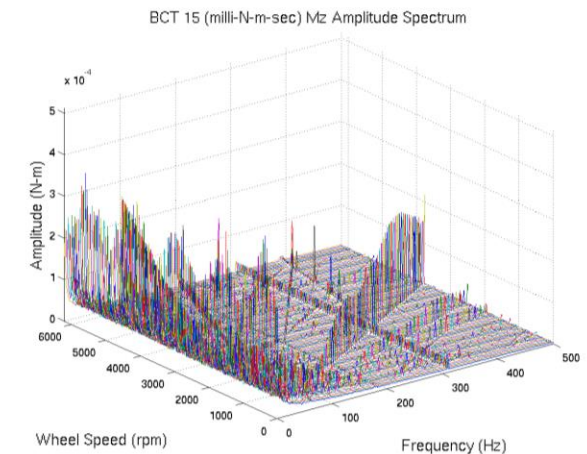
(c) M_x waterfall.



(d) M_y waterfall.

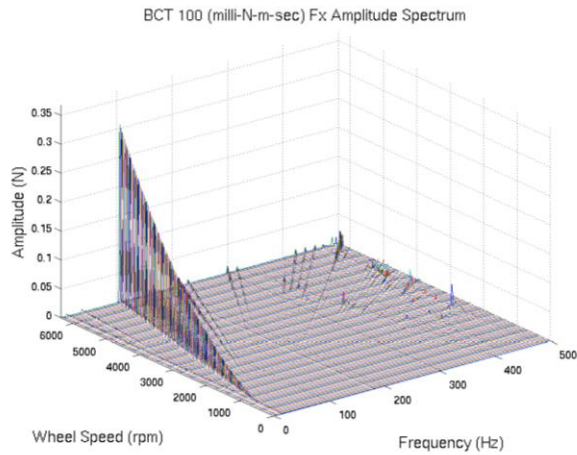


(e) F_z waterfall.

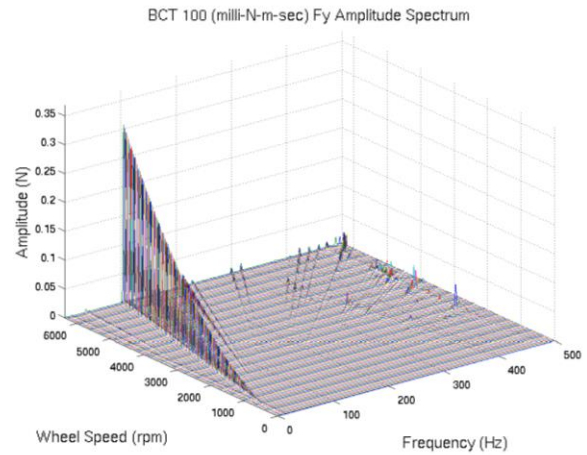


(f) M_z waterfall.

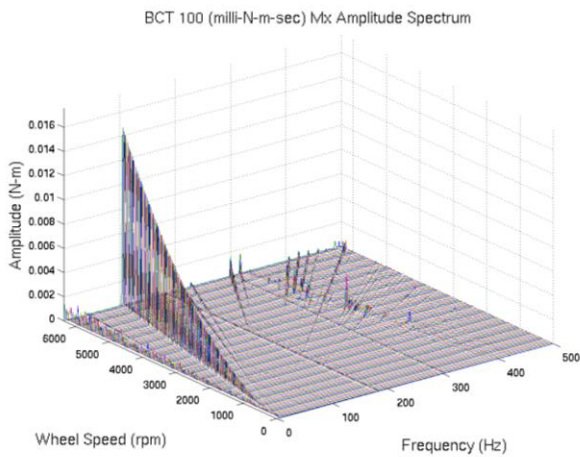
Figure 5. Waterfall plots for the BCT 15 reaction wheel. Exported forces and torques are characterized out to 500 Hz and up to 6200 RPM. The fundamental and the interaction of the harmonics with the rocking mode are clearly visible. The amplitudes of the F_z force and M_z moment are substantially smaller than the other components.



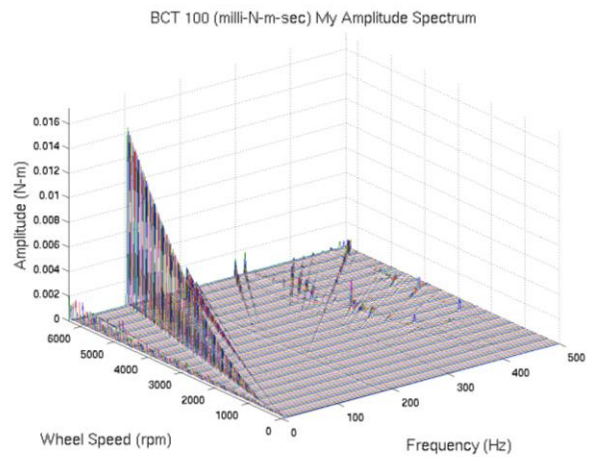
(a) F_x waterfall.



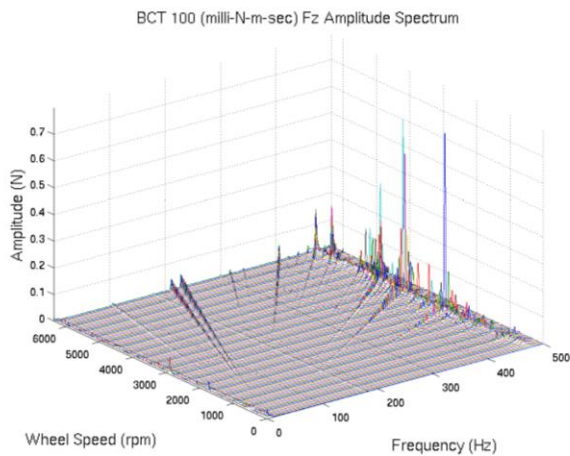
(b) F_y waterfall.



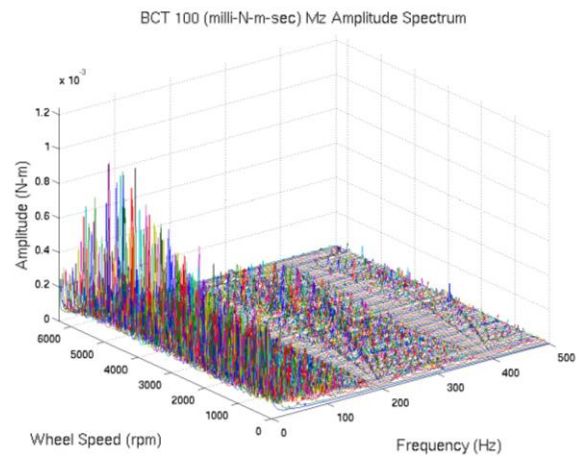
(c) M_x waterfall.



(d) M_y waterfall.

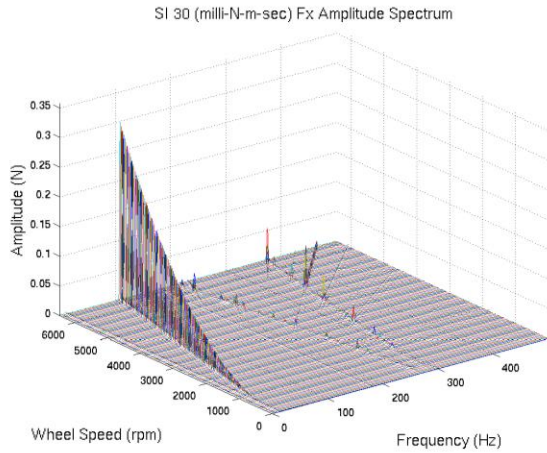


(e) F_z waterfall.

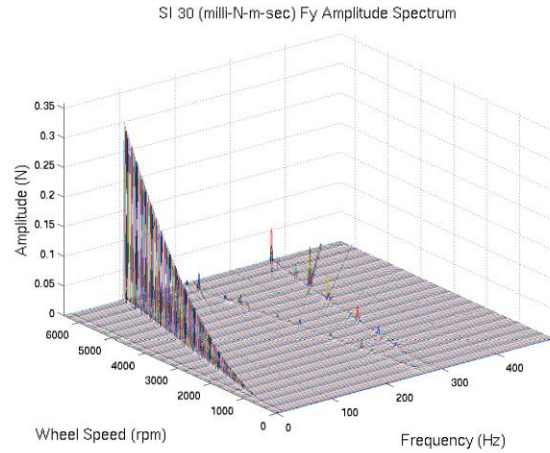


(f) M_z waterfall.

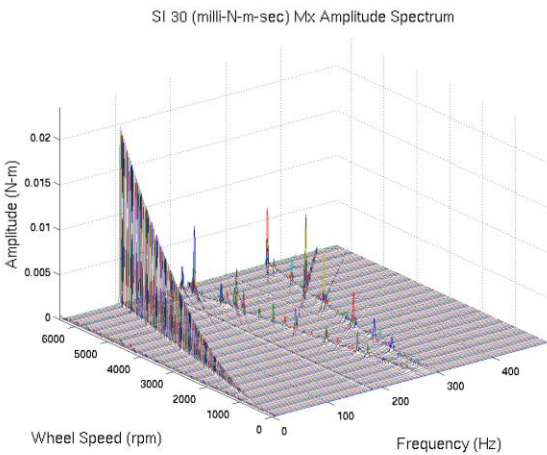
Figure 6. Waterfall plots for the BCT 100 reaction wheel. Maximum wheel speed for this motor was 6350 RPM. Rocking modes are diminished as compared to the BCT 15 wheel. A radial translation mode can be seen in the F_x and F_y plots at ~ 480 Hz. A large axial translation mode can be seen at the same frequency in the F_z plot.



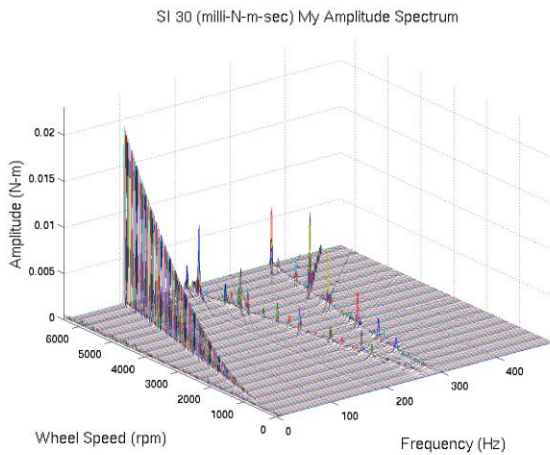
(a) F_x waterfall.



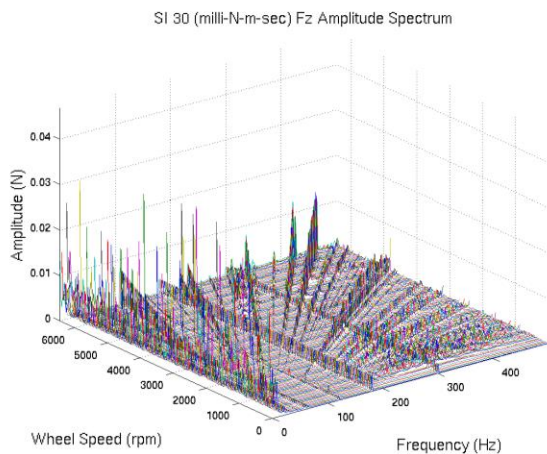
(b) F_y waterfall.



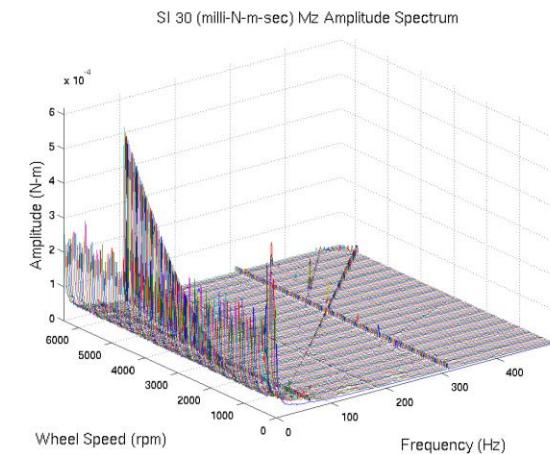
(c) M_x waterfall.



(d) M_y waterfall.



(e) F_z waterfall.



(f) M_z waterfall.

Figure 7. Waterfall plots for the SI 30 reaction wheel. Maximum wheel speed for this motor was 6450 RPM. Axial and radial translation modes cannot be seen in any of the waterfall plots for this reaction wheel. Again the F_z and M_z plots are substantially smaller than the other signals. Seismic and line background noises are the same order of magnitude as the F_z and M_z signals.

of high frequency disturbances can have an appreciable effect on instrument pointing, however, since damping and modes of the spacecraft structure come into play in this circumstance. The lower damping of the BCT wheels relative to the SI wheel is due to a diaphragm flexure used to preload the bearings. Apparently, this preload design avoids reliability issues with conventionally (wave spring) preloaded bearings, but does decrease the damping. As previously mentioned, BCTs new generation of the reaction wheels incorporate a visco-elastic damped isolator between the wheel and the housing that should improve the structural cage mode performance of the reaction wheel structure with the added reliability of their preload design (Steg, S.: private communication, August 2015). The Sinclair wheel uses damping in the form of a preloaded silicone O-ring (Sinclair, D.: private communication, July 2015).

Given the effect that structural cage modes can have on the disturbance signals produced by a reaction wheel, one important design consideration for any reaction wheel is to make sure that the rocking mode does not intersect the fundamental harmonic below the maximum wheel speed. None of the CubeSat scale reaction wheels tested in this paper have this defect, but larger wheels produced by Ithaco do exhibit this problem (Masterson, 1999).

Tables 2 and 3 list a modal summary of the reaction wheels and the modeled harmonic coefficients for

each wheel. Many more harmonics exist, but the ones listed in Table 3 are those judged to be the most prominent by their brightness in the contour plot. These coefficients are the h_i values used in Eqs. 7–12. The fundamental is represented by the coefficient closest to 1.0. Very few of these coefficients are octaves, or integer multiples, of the fundamental, implying that bearing imperfections play an important role in describing the complete behavior of these devices.

The data used to generate the waterfall plots discussed above was subsampled at 1000 Hz. If the data is not subsampled, waterfall plots up to 50 kHz can be generated. This was done for the F_x signal of the BCT 100 wheel. The 20 kHz PWM signal for this wheel showed up in the waterfall plot, which was likely due to high frequency coupling between the M_z torque and F_x direction. The torque produced by the PWM signal is also modulated by the ripple torque of the motor, the frequency of which depends on the wheel speed. Since the BCT 100 wheel has 14 poles, one would expect to see energy at both the sum and difference of the PWM frequency and ripple torque frequency. This is exactly what the full spectrum waterfall plot revealed. In addition, the waterfall plot also had harmonics of the sum and difference, since both the PWM and ripple torques are non-sinusoidal.

Table 2. Modal Summary for Reaction Wheels

Wheel	Rocking Mode	Axial Translation	Radial Translation	Number of Modeled Harmonics
BCT 15	300 Hz	380 Hz	NA	23
BCT 100	400 Hz	480 Hz	480 Hz	38
SI 30	290 Hz	NA	NA	27

Table 3. Summary of Reaction Wheel Harmonic Coefficients

Wheel	Harmonic Coefficients: (Sorted lowest to highest)
BCT 15	0.9999 1.5457 1.9997 2.4345 2.5497 2.9953 3.0904 3.4463 3.5441 3.9978 4.0824 4.5502 4.9911 5.0923 5.4437 6.0923 6.5043 7.1050 7.9276 8.5401 10.2416 12.7994 14.8571
BCT 100	0.3605 0.7206 0.9997 1.4413 1.6381 1.8273 1.9994 2.1648 2.3165 2.5098 2.8335 2.9986 3.2235 3.4610 3.5810 3.6570 3.8342 3.9986 4.1637 4.3294 4.4687 4.6296 4.8310 4.9964 5.1580 5.6652 5.8299 5.9962 6.1332 6.4473 6.6151 6.7288 7.6659 8.6558 9.6270 10.4109 11.4971 12.4719
SI 30	1.0120 2.0240 2.1563 2.2462 2.5181 2.7652 2.9006 3.2366 3.4852 3.5992 3.9575 4.3188 4.6926 4.9254 5.0486 5.8648 6.1093 6.2523 6.45760 6.6036 6.7870 8.1606 8.8814 9.6069 10.7256 12.8661 16.1864

4.1. ASTERIA Mission Results

Reaction wheel disturbance models are an essential part of an error budget for any mission that has tight pointing requirements (Lucke et al., 1992). The Arcsecond Space Telescope Enabling Research in Astrophysics (ASTERIA) mission requires 5.0 arcsecond RMS stability over a period of 20 minutes. Given the relatively small inertia of this spacecraft (the spacecraft is approximately $10 \times 20 \times 30$ cm and 10 kg), it is important to know how much the reaction wheel disturbances affect the pointing. A frequency-domain analysis was performed to determine the pointing jitter from the reaction wheels as a function of wheel speed. Since the wheel speeds generate high-frequency disturbances, no attenuation from the ACS loop was assumed in this analysis.

The first step in this process is to determine the input disturbance power spectral density generated by the reaction wheels. The ASTERIA mission uses three orthogonal BCT15 wheels. The reaction wheel disturbance frequencies are tied to the wheel speed, which are likely to be different for the three wheels and will change over time due to maneuvering and momentum buildup from external disturbances. To simplify this analysis, it will be assumed that the three wheels are at the same, constant wheel speed. This wheel speed will then be varied to determine how the pointing jitter changes as a function of wheel speed. The one-sided power spectral density of the reaction wheel disturbance force, $F_x(t)$, can be written as:

$$P_{F_x}(f) = \sum_{i=1}^{N_h} \frac{F_{x_i}^2(\Omega)}{2} \delta(h_i\Omega - f) \quad (13)$$

where $\delta(\cdot)$ is the Dirac delta function. Similar expressions can be written for the other two forces and additional three moments. For a given wheel, RW_i , these can then be gathered into a vector quantity:

$$P_{RW_i}(f) = \left[P_{F_x}(f) P_{F_y}(f) P_{F_z}(f) P_{M_x}(f) P_{M_y}(f) P_{M_z}(f) \right]^T \cdot (14)$$

In practice, these power spectral densities will have a discrete frequency grid and will be integrated numerically to determine the RMS pointing error. Therefore, the continuous Dirac delta function can be replaced by a discrete Kronecker delta function. The exact location of each Kronecker delta may need to be rounded to the closest frequency grid point, depending on how the frequency grid is selected. Also, the amplitude of the Kronecker deltas must be chosen such that the cumulative numerical integral over frequency matches the cumulative integral of the continuous power spectral density. The amplitudes will therefore depend on the frequency grid and the type of numerical integration that is performed.

To determine the effect that these input disturbance power spectral densities have on pointing of the spacecraft's payload, the transfer functions from each of the reaction wheel disturbances to each of the three payload pointing axes must be determined. This is typically done through a normal modes analysis of the finite-element model (FEM) of the spacecraft. The mode frequencies and mode shapes from this analysis, along with an estimate of the modal damping, can be used to construct a state-space model of the flexible dynamics of the spacecraft. Note that this model contains important mass properties of the system such as mass, inertia, and the location of each reaction wheel node relative to the spacecraft center of mass. If the flexible-body state-space model determines the movement of individual optical elements, instead of the payload as a whole, an optical sensitivity matrix can be used to convert the translations and rotations of each optical element into the resulting effect on payload pointing.

Figure 8a shows the frequency response from reaction wheel torques to payload pointing for ASTERIA. The first two modes are a large X-axis mode around 29 Hz and a Y-axis mode around 82 Hz. Note that this figure only shows three of the nine transfer functions for torque (the cross-axis transfer functions are not shown). In addition, the nine transfer functions for force are also not shown.

With the input disturbance power spectral densities and the transfer functions, the pointing power spectral density can be determined with the following equation:

$$\mathbf{P}_{SC}(f) = \sum_{i=1}^3 |\mathbf{G}_{SC \leftarrow RW_i}(f)|^2 {}^{SC}\mathbf{T}^{RW_i} \mathbf{P}_{RW_i}(f), \quad (15)$$

where $\mathbf{P}_{SC}(f)$ is a 3×1 vector containing the X, Y, and Z components of the spacecraft pointing power spectral density, $\mathbf{G}_{SC \leftarrow RW_i}(f)$ is a 3×6 transfer function matrix from RW_i force and torque input to pointing output, and ${}^{SC}\mathbf{T}^{RW_i}$ is a 6×6 block diagonal matrix that transforms the force and torque vectors from the RW_i frame to the SC frame. The notation $|\cdot|^2$ denotes the element-by-element magnitude squared of each of the elements in the transfer function matrix. This equation was derived from the input-output relationship of power spectral densities (Wirsching et al., 1995). Note that adding the resulting pointing power spectral densities for each of the reaction wheels is equivalent to taking the sum of squares of the RMS of each of the reaction wheel power spectral densities.

The square root of the integral of the pointing power spectral density, given by Eq. 15, over all frequencies gives the root-mean-square (RMS) pointing error. Figure 8b shows the resulting RMS pointing error for each axis as a function of wheel speed for ASTERIA. The pointing error consists of a base pointing error with superimposed peaks. The base pointing error of approximately 0.1 arcsec RMS is due to the static and dynamic imbalances interacting with the

rigid inertia of the spacecraft. The large peak in pointing error of 8.0 arcsec RMS about the X-axis at around 1750 RPM is due to the static and dynamic imbalance disturbances of all three wheels exciting the structural mode on the spacecraft at 29 Hz. This is a conservative pointing error estimate, since it assumes all three wheels are at the same speed, exciting a structural mode with a low damping of 0.25 percent. In addition, these results do not include the effect of BCT’s viscoelastic dampers, which are present in ASTERIA’s configuration. It should also be noted that this resonance is about the payload roll axis, which is less sensitive than the other two axes. The amount of jitter produced by these wheels is low enough to meet ASTERIA’s arcsecond-level pointing requirements.

This analysis provides a very detailed view of how the reaction wheel disturbances can affect the pointing of a spacecraft. It shows that reaction wheel disturbances, especially when they interact with structural modes, can have a large impact on pointing. This may feed into design iterations that address the structural resonances or operational constraints on the allowable wheel speeds during times when high-precision pointing is required. It must be noted that reaction wheel disturbances are just one source of error in a larger pointing budget. How the reaction wheel disturbances are handled depends on how much they contribute to pointing error relative to other sources in the error

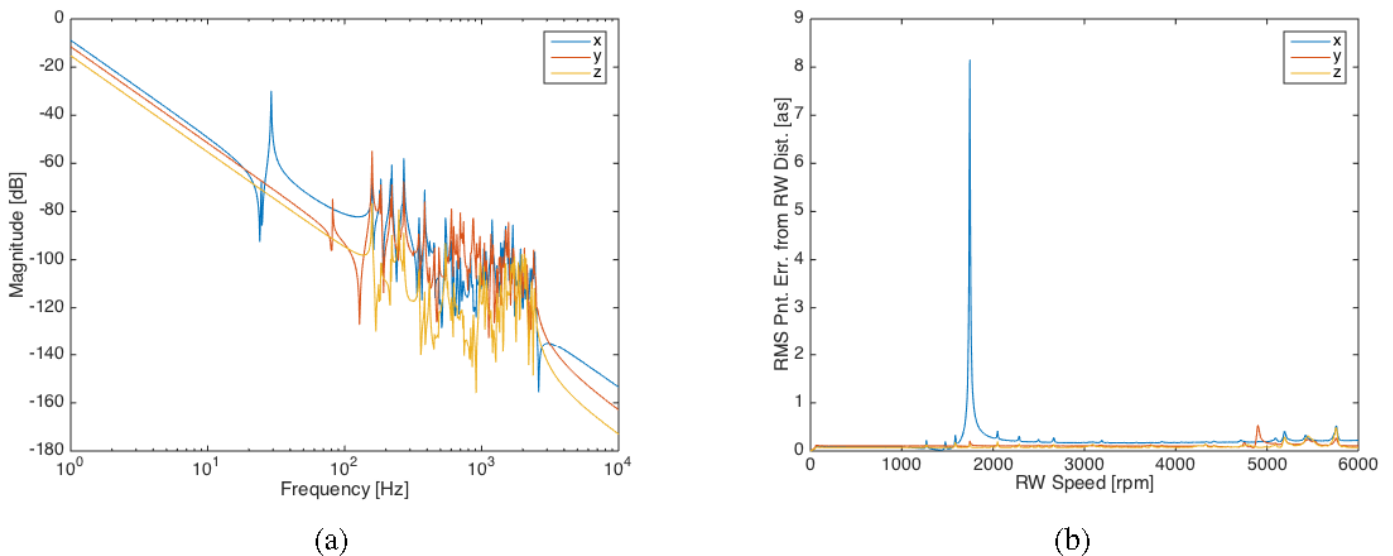


Figure 8. (a) Frequency response of the ASTERIA spacecraft from X, Y, Z reaction wheel torque to X, Y, Z payload pointing. (b) Contribution to ASTERIA pointing error from three BCT 15 wheels, as a function of wheel speed, run through the ASTERIA finite-element model.

budget. The above analysis assumes a steady state wheel speed; transient jitter performance is not addressed. It also ignored gyroscopic stiffening of the structure caused by the rotating flywheels of each reaction wheel. Furthermore, the forces and torques used in the reaction wheel model were determined using the stiff impedance of the dynamometer. When the wheels are mounted in the flexible structure of the Spacecraft, the forces and torques are likely to be reduced. In this sense, the analysis presented above can be considered as a worst case.

5. Conclusions

This paper has discussed the testing and characterization of three different CubeSat reaction wheels. To review, the harmonic coefficients were selected using contour plots. This interactive procedure allowed for the use of engineering judgment in selecting only the most prominent harmonics. Many of the less significant harmonics are omitted in this way. Automated methods, such as using the Hough transforms or correlation methods to identify harmonics, proved less reliable. The estimation of the harmonic coefficients was then refined, using a least squares solution. The amplitudes for each harmonic were then extracted from the waterfall plots, which completes the model. The dynamometer data used to model the wheels was corrupted by seismic, line, and other electronic sources which contributed to the noise floor. Efforts were made to eliminate these noise sources using a polynomial fit of the low wheel speed data.

This type of testing has been done for larger reaction wheels that are used in conventionally sized spacecraft, but to the knowledge of the authors, this is the first attempt to model and compare multiple reaction wheel disturbance profiles for wheels of this size class. This testing revealed a plethora of harmonics with amplitudes that can be as large as the fundamental harmonic when they interact with the structural cage modes of the wheel assembly. The large number of harmonics is likely due to imperfect bearing manufacturing tolerances. The testing also revealed that the two BCT wheels tested had larger than expected dynamic imbalances and structural cage modes. The fine balancing option for the BCT 100 wheel made the

static and dynamic imbalances quite a bit less than would be expected based on its larger momentum capacity.

As an example of the type of analysis that can be done with the models developed in this paper, the exported forces and torques of the BCT 15 reaction wheel model were incorporated into a FEM and used to predict the pointing performance for the ASTERIA mission. In addition to performance prediction, this type of analysis can be used to make system level trades and to impose operational constraints if needed.

Acknowledgments

The work described in this paper was carried out at the Jet Propulsion Laboratory, California Institute of Technology, under contract with the National Aeronautics and Space Administration. The authors wish to thank Rebecca Masterson and Scott Ploen for their helpful discussions.

References

- Bialke, B. (1998): High Fidelity Mathematical Modeling of Reaction Wheel Performance, in *Advances in the Astronautical Sciences*, pp. 483–496, Breckenridge, CO.
- de Weck, O. (1998): *Reaction Wheel Disturbance Analysis, Tech. Rep. MIT-SSL-NGST-98-1*, Massachusetts Institute of Technology, Research Contract No. NAG5-6079.
- Elias, L., Dekens, F., Basdogan, I. et al. (2003): Methodology for Modeling the Mechanical Interaction Between a Reaction Wheel and a Flexible Structure, in *SPIE Proceedings, Interferometry in Space*, pp. 541–555, Waikoloa, HI.
- Liu, K. C., Maghami, P., and Blaurock, C. (2008): Reaction Wheel Disturbance Modeling, Jitter Analysis, and Validation Tests for Solar Dynamics Observatory, in *AIAA Guidance, Navigation, and Control Conf.*, pp. 1–18, Honolulu, HI.
- Lucke, R., Sirlin, S., and San Martin, M. (1992): New Definitions of Pointing Stability -AC and DC Effects, *J. Astronautical Sciences*, vol. 40, pp. 557–576.

Macala, G. (1997): *Cassini Reaction Wheel Model, Tech. rep.*, Jet Propulsion Laboratory, Cassini Control Analysis Book: Vol. III.

Masterson, R. (1999): Development and Validation of Empirical and Analytic Reaction Wheel Disturbances and Models, Master's thesis, Department of Aeronautics and Astronautics, Massachusetts Institute of Technology, Cambridge, MA.

Masterson, R., Miller, D., and Grogan, R. (2002): Development and Validation of Reaction Wheel Disturbance Models: Empirical Model, *J. Sound and Vibration*, Vol. 249(3), pp. 575–598.

Neat, G., Melody, J., and Lurie, B. (1998): Vibration Attenuation Approach for Spaceborne Optical Interferometers, *IEEE Transactions on Control Systems Technology*, Vol. 6(6), pp. 689–700.

Pong, C., Smith, M., Knutson, M. et al. (2011): One-Arcsecond Line-of-Sight Pointing Control on Exoplanet-Sat, in *Advances in the Astronautical Sciences*, pp. 147–166, Breckenridge, CO.

Sinclair, D., Grant, C., and Zee, R. (2007): Enabling Reaction Wheel Technology for High Performance Nanosatellite Attitude Control, presented at the 21st Annual AIAA/USU Conf. on Small Satellites, Logan, UT, August 5–10, 2007, Paper SSC07-X-3.

Wirsching, P., Paez, T., and Ortiz, K. (1995): *Random Vibrations: Theory and Practice*, 1st ed., New York, NY: John Wiley and Sons Inc.